

# Revealing the Mechanics of Helicoidal Composites through Additive Manufacturing and Beetle Developmental Stage Analysis

Alireza Zaheri, Joel S. Fenner, Benjamin P. Russell, David Restrepo, Matthew Daly, Di Wang, Cheryl Hayashi, Marc A. Meyers, Pablo D. Zavattieri, and Horacio D. Espinosa\*

Investigation into the microstructure of high performance natural materials has revealed common patterns that are pervasive across animal species. For example, the helicoid motif has gained significant interest in the biomaterials community, where recent studies have highlighted its role in enabling damage tolerance in a diverse set of animals. Moreover, the helicoid motif corresponds to a highly adaptable architecture where the control of the pitch rotation angle between fibrous structures produces large changes in its mechanical response. Nature, takes advantage of this special feature enabling an active response to particular biological needs occurring during an animal's ontogeny. In this work, we demonstrate this adaptive behavior in helicoidal architectures by performing a mechanistic analysis of the changes occurring in the cuticle of the figeater beetle (*Cotinis mutabilis*) during its life cycle. We complement our investigation of the beetle with the testing of 3D printing samples and a systematic analysis of the effect of pitch angle in the inherent mechanics of helicoidal architectures. Experimentation and analysis reveal improved isotropy and enhanced toughness at lower pitch angles, highlighting the flexibility of the helicoidal architecture. Moreover, trends in stiffness measurements were found to be well-predicted by laminate theory, suggesting facile mechanics laws for use in biomimicry.

limited selection of base constituents. Indeed, biological materials often exhibit synergistic behaviors, whereby their mechanical performance exceeds the anticipated limitations set by their constituents. In this regard, the unique mechanical properties observed in Nature stem from synergistic interactions between distinct structural features ranging from the nano- to microscopic scales.<sup>[1]</sup> Interestingly, these hierarchical designs have enabled biological materials that achieve multifunctional behaviors not observed in common engineering materials. For instance, several examples have been reported of natural materials exhibiting unusual combinations of lightweight, high strength, and high toughness properties.<sup>[2]</sup> In contrast, engineering materials often exhibit an inverse relationship between these desired properties.<sup>[1a]</sup> Uncovering how Nature employs different strategies to achieve these features presents a tempting route for the design of high performance engineered materials and systems. In this

regard, improvements in analytical technologies, such as the emergence of increasingly powerful forms of microscopy, and recent advances in nanoscale mechanical experimentation have provided powerful tools for investigators to uncover the multi-scale design schemes in numerous biological organisms.<sup>[3]</sup>

## 1. Introduction

Nature has evolved efficient strategies to develop biological materials with exceptional mechanical properties from a

A. Zaheri, Prof. H. D. Espinosa  
Theoretical and Applied Mechanics Program  
Northwestern University  
Evanston, IL 60208, USA  
E-mail: espinosa@northwestern.edu


Dr. J. S. Fenner, Dr. D. Restrepo, Dr. M. Daly, Prof. H. D. Espinosa  
Department of Mechanical Engineering  
Northwestern University  
Evanston, IL 60208, USA

Dr. B. P. Russell  
Department of Engineering  
University of Cambridge  
Cambridge CB2 1PZ, UK

D. Wang, Prof. P. D. Zavattieri  
Lyles School of Civil Engineering  
Purdue University  
West Lafayette, IN 47907, USA

Prof. C. Hayashi  
Division of Invertebrate Zoology  
American Museum of Natural History  
New York, NY 10024, USA

Prof. M. A. Meyers  
Department of Mechanical and Aerospace Engineering  
Materials Science and Engineering Program  
University of California  
San Diego, La Jolla, CA 92093, USA

 The ORCID identification number(s) for the author(s) of this article can be found under <https://doi.org/10.1002/adfm.201803073>.

DOI: 10.1002/adfm.201803073

Biological materials are often present as composite structures, where soft (i.e., polymeric materials) and hard (i.e., mineralized materials) constituents are mixed under different organizational formats to generate specific functionalities. Typically, the hard phase acts as a reinforcement, and is distinguishable as continuous and discontinuous fibers, platelets or particulates.<sup>[4]</sup> Among these reinforcements, fibers have been found to be the most abundant in Nature, and are available in composites with unidirectional,<sup>[5]</sup> orthogonal,<sup>[6]</sup> and helicoidal arrangements.<sup>[7]</sup> Recently, helicoidal composites have been identified as one of the most common architectural motifs found in Nature, showing prevalence in diverse taxonomic groups including fish, plants, and arthropods.<sup>[8]</sup> Helicoidal composites are characterized by the stacking of fibrous layers rotated by a constant pitch angle ( $\gamma$ ), as shown in Figure 1a. The seminal work in helicoidal structures is attributed to Yves Bouligand, who used scanning electron microscopy to analyze the cuticle of four crab species. By inspecting oblique sections of the cuticles, Bouligand observed that the fibers followed a curved pattern, and concluded that this pattern can be rationalized as a structure of overlapping planes of fibrils rotated by small angles about a common axis.<sup>[9]</sup> Since this study, multiple researches have used several techniques to observe helicoidal structures in biological materials including polarized microscopy,<sup>[10]</sup> X-ray scattering,<sup>[11]</sup> and recently, Espinosa and co-workers<sup>[12]</sup> employed atomic force microscopy and contact mechanics to identify the helicoidal geometry and anisotropic elastic constants of nanofibers in the exoskeleton of beetles.

Helicoidal structures have been related to interesting mechanical properties observed in Nature. For instance, recent studies have shown that the cuticle of a number of arthropods exhibit remarkable toughness and damage resistance despite their weak constituent materials.<sup>[13]</sup> These features have been associated with the presence of a helicoidal fibrous composite as the main architecture forming the cuticle. Helicoidal fibrous composites provide an enhanced fracture toughness by forcing a twisting interface along the direction of the crack front.<sup>[14]</sup> Consequently, this crack deflection enforces mode mixity and amplifies the surface area per unit required for a crack propagate through the structure.<sup>[15]</sup> Another interesting functionality observed in Nature, corresponds to the utilization of the helicoidal motif as a flexible architecture where the

orientation of fibrous structures may be altered to adapt to particular biological needs during an animal's ontogeny. For example, the life cycle of the figeater beetle (*Cotinis mutabilis*) comprises a complete metamorphosis of the organism, consisting of four distinct developmental stages: namely, the egg, larval, pupal, and adult stages, as illustrated in Figure 1b. At all post-hatch life stages (e.g., larva, pupa, and adult), the cuticle of figeater beetle is comprised of chitinous fibers in a helicoidal arrangement with a relatively low mineralization

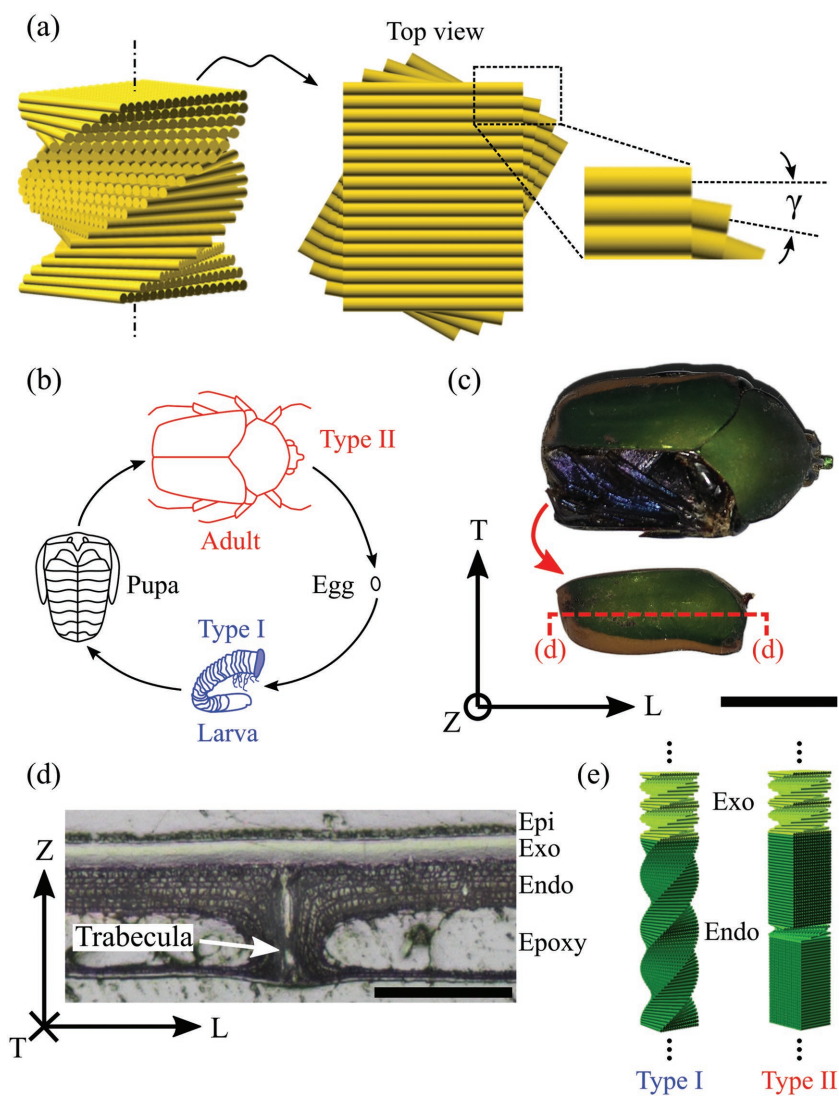


**Figure 1.** a) Schematic representation of the helicoidal architecture. b) A schematic of the typical life cycle of the figeater beetle highlighting the animal's morphology as it transitions from egg to adult. c) A photograph of an adult figeater beetle (*Cotinis mutabilis*) with an elytron removed to expose the underlying soft-tissue primary flight wing. The removed elytron is positioned below the beetle. The red dashed line indicates the orientation of the cross-section shown in (d). The transverse (T), longitudinal (L), and out-of-plane (Z) coordinate axes are provided. The scale bar represents 1 cm. d) An optical micrograph showing the cross-section of the adult elytron monocoque shown in (b). The epi-, exo-, and endocuticle layers are indicated. The region labeled as epoxy is hollow in vivo. The scale bar represents 100  $\mu\text{m}$ . e) A schematic showing the helicoidal structures of the exo- and endocuticles in the epidermis of the figeater beetle larva (Type I) and the helicoidal and pseudo-orthogonal architecture in the adult beetle elytron (Type II).

content (<10% mineralization by weight<sup>[16]</sup>). The architecture of the cuticle is heterogeneous and is composed of layers that possess a distinct helicoidal organization of chitinous fibers. These domains are referred to as the epi-, exo-, and endocuticles in sequence progressing from the dorsal surface of the structure. In the larva stage, this cuticle serves as the epidermal layer of the organism. In the adult figeater beetle the helicoidal architecture is evident in the elytra, which are a dermal shell that serve two roles—namely as protection for the underlying soft-tissue wings, and as secondary wings that generate flapping forces during flight. In contrast to the epidermis of the larva, the ventral membrane of the adult elytron encloses a sizeable hollow region that is connected to the various cuticle layers through a trabecular. This structure is pseudo-monocoque in design, thus providing both weight-savings and bending rigidity to the elytron for improved mechanical and flight performance. Figure 1c depicts an adult figeater beetle with one of the elytra removed to expose a soft-tissue wing. Figure 1d provides an optical micrograph of a cross-section of an adult figeater beetle elytron, which clearly illustrates the different cuticle layers.

A specific aspect of the cuticle architecture that is modulated during the developmental stages of the figeater beetle is the organization of fibers in the procuticle (i.e., exo- and endocuticle layers). In the larva procuticle (referred to as Type I), the exo- and endocuticles are distinct helicoidal structures with different pitch angles ( $\gamma_{ex}$  and  $\gamma_{en}$ ). By comparison, the procuticle (referred to as Type II) of the adult elytron possesses the same helicoidal structure as the larva in its exocuticle layer. However, during the life cycle of the animal, the endocuticle structure transitions from a helicoidal to a pseudo-orthogonal architecture.<sup>[17]</sup> In this pseudo-orthogonal architecture, alternating layers of orthogonally aligned fibers are stacked to form the structure of the endocuticle.<sup>[18]</sup> Interfacing between these orthogonal layers is facilitated by a thin helicoidal transition zone with a pitch angle,  $\gamma_{tz}$ .<sup>[19]</sup> The different architectures of the procuticle in the larva epidermis and adult elytron are illustrated schematically in Figure 1e. These changes in the cuticle architecture, have profound implications in its biological role as its function transitions during the animal's lifetime—from serving primarily as protection against predation in the larva stage, toward a mixed functionality that balances protection with flight mechanics in the adult stage.

In this work, using a mechanistic analysis, we explore life-cycle transitions in the helicoidal architecture of the figeater beetle. In particular, we emphasize the structural changes observed in the epidermis of the larva when compared against the elytra of the adult beetle with a focus on the changing biological role of each structure, and we draw a connection between the mechanics of the helicoidal structure and its role in multifunctional natural materials. We complement this mechanistic analysis with 3D printed samples to perform a systematic analysis of the effect of pitch angle in the inherent mechanics of the helicoidal structures. The findings of this study are discussed within the context of the development of efficient structural fibrous composite systems with tunable mechanical properties.

## 2. Helicoidal Structures as a Flexible Multifunctional Architecture

Given the relatively few constituents available for the assembly of biological systems, Nature leverages architecture to produce multifunctional materials. The utilization of the helicoidal motif as an adaptable architecture is particularly evident in arthropods, where the orientation of fibrous structures may be altered to adapt to particular biological needs during an animal's ontogeny. To illustrate the functional flexibility of the helicoidal architecture, we perform a mechanics analysis of helicoidal structures in the epidermal cuticle of the figeater beetle (*Cotinis mutabilis*) during two stages of its life cycle—namely, the larva and adult stage.

As discussed in the previous section, the epidermis of the beetle is comprised of multiple stackings of helicoidal architectures with varying pitch angles. In addition, the cuticle architecture is modulated during developmental stages of the figeater beetle changing from Type I to Type II. In the Type I configuration the cuticle serves primarily as a protection mechanism against predation in the larva stage, whereas the Type II configuration exhibits a mixed functionality that balances protection with flight mechanics in the adult stage. In the following subsections, the mechanical properties and fracture toughness of the Type I and Type II procuticle architectures are discussed in order to highlight the role of structure in modulating mechanical performance during the life cycle of the figeater beetle.

### 2.1. Comparison of Procuticle Stiffness in the Life Cycle of the Figeater Beetle

The adult figeater beetle possesses two sets of wings that are attached to its dorsal anterior: the primary soft-tissue wings, and the elytra. During rest, the soft-tissue wings are folded underneath the protective elytra, whereas in flight both sets of wings are extended and achieve lift through a synchronized flapping.<sup>[20]</sup> The dual roles of the elytron (i.e., protective and synchronized flapping) require that it possesses a high stiffness such that it is resistant to puncture from predation and that deformations induced by aerodynamic loadings remain small to avoid collision with the primary wings during flight. From a mechanics perspective, the flexural and torsional stiffnesses of the elytron are largely defined by the properties of the procuticle, which represents the vast majority of material positioned away from the neutral axis of the monocoque.

The elastic properties of the procuticle may be estimated by treating its helicoidal components as a multidirectional laminate comprised of a helical stacking of fiber-reinforced lamina. Figure 2 illustrates the hierarchy of structures (i.e., lamina → laminate → procuticle) that comprise the epidermal layers of the figeater beetle. Under an assumption of thin layers (i.e., plane stress), the orthotropic stiffness tensor of a lamina in the material coordinate system takes the form<sup>[21]</sup>

$$Q = \begin{bmatrix} \frac{E_1}{1 - \nu_{12}\nu_{21}} & \frac{\nu_{12}E_2}{1 - \nu_{12}\nu_{21}} & 0 \\ \frac{\nu_{21}E_1}{1 - \nu_{12}\nu_{21}} & \frac{E_2}{1 - \nu_{12}\nu_{21}} & 0 \\ 0 & 0 & G_{12} \end{bmatrix} \quad (1)$$

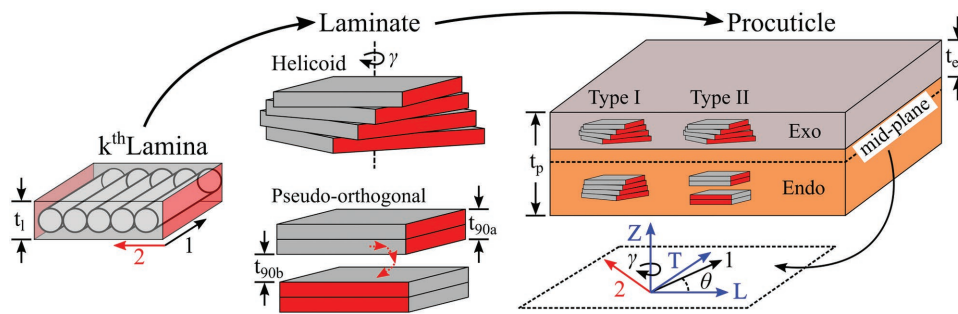


**Figure 2.** The hierarchy of structures that comprises the procuticle of the figeater beetle. Individual lamina are stacked in a helicoidal or pseudo-orthogonal arrangement to form laminates. The laminate structures of the exo- and endocuticles constitute the procuticle of the figeater beetle. The parameters defined here are used in the mechanics analysis to determine the homogenized mechanical properties of the Type I and Type II procuticles. The fiber (1) and transverse (2) material directions as well as the global ( $L$ - $T$ - $Z$ ) coordinate frame are depicted in the image. The orientation relationship between the material and global frames is described by  $\theta$ , which is a function of position ( $Z$ ) from the mid-plane of the procuticle.

where  $E$ ,  $G$ , and  $\nu$  are the elastic and shear moduli, and the Poisson's ratio, respectively. These parameters are indexed relative to the fiber (1) and transverse (2) material directions (see Figure 2). It should be noted that the components of the stiffness tensor ( $Q$ ) represent the in-plane coefficients of the 3D orthotropic stiffness tensor under a plane stress simplification. The components of  $Q$  may be transformed into the procuticle frame (i.e.,  $L$ - $T$ ) through consideration the relative rotation of the fiber axis in the lamina ( $\theta$ ) as a function of position ( $Z$ ) from the midplane of the structure. This relationship is dependent on the type of procuticle (i.e., Type I or Type II) and on the constitutive laminate structures (i.e., helicoidal or pseudo-orthogonal). Using the physical parameters defined in Figure 2, the orientation of the fiber axis for the Type I and Type II procuticles ( $\theta_I$  and  $\theta_{II}$ ) may be described by the following piecewise continuous relationships:

$$\theta_I(Z, \gamma) = -\frac{\gamma}{t_1} \left( Z - \frac{t_p}{2} \right), \quad \text{where } \gamma = \begin{cases} \gamma_{ex}, & Z \geq t_p/2 - t_{ex} \\ \gamma_{en}, & Z < t_p/2 - t_{ex} \end{cases} \quad (2a)$$

$$\theta_{II}(Z, \gamma = \{\gamma_{ex}, \gamma_{tz}\}) = \begin{cases} -\frac{\gamma_{ex}}{t_1} \left( Z - \frac{t_p}{2} \right), & Z \geq t_p/2 - t_{ex} \\ \in \{0, 90, \theta_{tz}(Z, \gamma_{tz})\}, & Z < t_p/2 - t_{ex} \end{cases} \quad (2b)$$

where  $t_1$ ,  $t_{ex}$ , and  $t_p$  are the thicknesses of the lamina, exocuticle, and procuticle, respectively. In this formulation, the lamina fibers are assumed to be aligned to the longitudinal axis at the dorsal surface of the exocuticle (i.e.,  $Z = t_p/2$ ). The orientation of the pseudo-orthogonal laminate alternates between  $0^\circ$  and  $90^\circ$ , with a periodicity defined by the thickness  $t_{90a}$ . This modulation in lamina orientation is facilitated by a transitional helicoidal region over a thickness  $t_{90b}$  (see Figure 2). The evolution of lamina orientation in this transitional zone is described by  $\theta_{tz}$ , which possesses the same form as (2), with a commensurate offset to ensure smooth transitions between orthogonal stacks in the pseudo-orthogonal laminate. Using these relations for the lamina orientation, the transformed stiffness tensor ( $\bar{Q}^k$ ) may be calculated as  $\bar{Q}^k = (T^k)^{-1} Q (T^k)$ , where  $T^k$  is the transformation matrix that converts tensor components of the  $k_{th}$

lamina from the material to global frames. The entries of  $T^k$  are calculated based on Equations (2) and (3) for  $\theta_I$  and  $\theta_{II}$ .

Upon determination of  $\bar{Q}^k$ , the homogenized in-plane elastic moduli (i.e.,  $E_L$  and  $E_T$ ) of the procuticle may be directly calculated using standard laminate theory analysis.<sup>[21]</sup> Table 1 provides a summary of the parameters used to calculate the elastic properties of the Type I and Type II procuticles based on our recent work on the adult beetle elytra.<sup>[12]</sup> It should be noted that this calculation assumes the constituent properties (i.e.,  $E$ ,  $G$ , and  $\nu$ ) do not change during the beetle's lifecycle. However, we stress that this analysis reveals the range of modulation in properties and design flexibility of helicoidal architecture in natural systems. Executing the calculations reveals that the longitudinal and transverse moduli in each structure are approximately equivalent (i.e.,  $E_L \approx E_T = E$ ), due to the symmetry of the Type I and Type II structures. However, the Type II structure is in general anisotropic and this equivalency of moduli is a circumstance of the alignment of orthogonal laminates to the longitudinal and transverse axes. Based on the above formulation, the in-plane moduli for the Type I ( $E_I$ ) and Type II ( $E_{II}$ ) structures are determined to be 332 and 368 MPa, respectively. It should be noted that the Type I structure is nearly isotropic. Indeed, the Zener ratios (see ref. [22]) for the Type I and Type II structures are 1 and 0.61, respectively. These results demonstrate how the structure of the procuticle may be altered during the lifecycle of the figeater beetle in order to serve a particular biomechanical purpose. The isotropic mechanical response of the Type I

**Table 1.** Parameters for mechanics analysis of the Type I and Type II procuticles in the figeater beetle.

Mechanical properties	Geometric parameters [ $\mu\text{m}$ ]	Pitch angles [ $^\circ$ ]	
$E_1$ [MPa]	710	$t_1$ 0.02	$\gamma_{ex}$ 16.4
$E_2$ [MPa]	70	$t_{ex}$ 13.20	$\gamma_{en}$ 10.2
$G_{12}$ [MPa]	90	$t_p$ 43.80	$\gamma_{tz}^{a)}$ 12.9
$\nu_{12}$	0.30	$t_{90a}^{a)}$ 5.00	
$\nu_{21}$	0.03	$t_{90b}^{a)}$ 0.12	

<sup>a)</sup>Parameters required in the mechanics analysis of Type II only.

epidermis in the larval phase is sacrificed in order to create stiffer elytron components in the adult beetle. More specifically, the preferential arrangement of the endocuticle fibers along the longitudinal and transverse directions improves the bending and torsional stiffness of the elytron monocoque at the expense of in-plane isotropicity.

## 2.2. Role of the Helicoidal Structure in Mitigating Fracture

A common feature in the procuticles of the larva and adult figeater beetle is the structure of the exocuticle. In both the Type I and Type II structures, the exocuticle remains as a strictly helicoidal arrangement of chitinous fibers. A natural conclusion from the previous mechanics analysis is that the overall stiffness of the Type II structure would improve if the exocuticle in the adult elytron were also organized in a pseudo-orthogonal arrangement. The absence of such a reorganization highlights the dual biological roles of the elytron in the adult figeater beetle: namely, flight mechanics, and resistance to predation. The preservation of the exocuticle as a helicoidal structure reflects the latter of these two niches. For instance, assuming a predation event leads to the nucleation of a crack along the surface of the elytron. Propagation of this crack into the exocuticle under a global Mode I loading exposes the crack front to a twisted arrangement of reinforcing chitinous fibers—providing added toughening via mode mixity. As the matrix in the helicoidal structures of the species studied here is weaker than the fibers,<sup>[23]</sup> the crack can be assumed to propagate along a path commensurate to the fiber pitch via matrix fracture. The fracture mechanics of a twisting crack propagating in a helicoid structure was recently analyzed in the work of Suksangpanya et al.<sup>[14]</sup> This analytical framework is implemented here to examine crack propagation through the exocuticle of the figeater beetle. It should be noted that this analysis is based on linear elastic fracture mechanics (LEFM) theory, and therefore cannot capture inelastic toughening events around the crack tip. However, the application of LEFM here is intended for comparative purposes. In this regard, this analysis reveals the added toughening achieved through the mode mixity enforced by the geometry of the crack propagation path in comparison to purely Mode I fracture. **Figure 3a** illustrates a crack front impinging on the exocuticle of a figeater beetle. Assuming a plane strain condition, the ratio of the local ( $G_c$ ) and material ( $G_c^m$ ) critical energy release rates for a twisting crack under Mode I loading is given by<sup>[14]</sup>

$$\frac{G_c}{G_c^m} = \left[ C_1^2 + C_2^2 + \frac{1}{(1-\nu)} C_3^2 \right]^{-1} \quad (3)$$

where  $C_1$ ,  $C_2$ , and  $C_3$  are geometric coefficients that describe the mode mixity of the crack front as a function of its kink ( $\alpha$ ) and twist ( $\varphi$ ) angles relative to the global  $L$ - $T$ - $Z$  axes. In this formulation,  $\varphi$  represents the angle of twist about the  $Z$  axis, and  $\alpha$  is the kink angle between the projection of  $L'$  on the  $L$ - $Z$  plane and the  $L$  axis. Please note the axes referenced in this section have been rotated relative to the definitions in Section 2.1. **Figure 3b** shows a schematic of a twisting crack

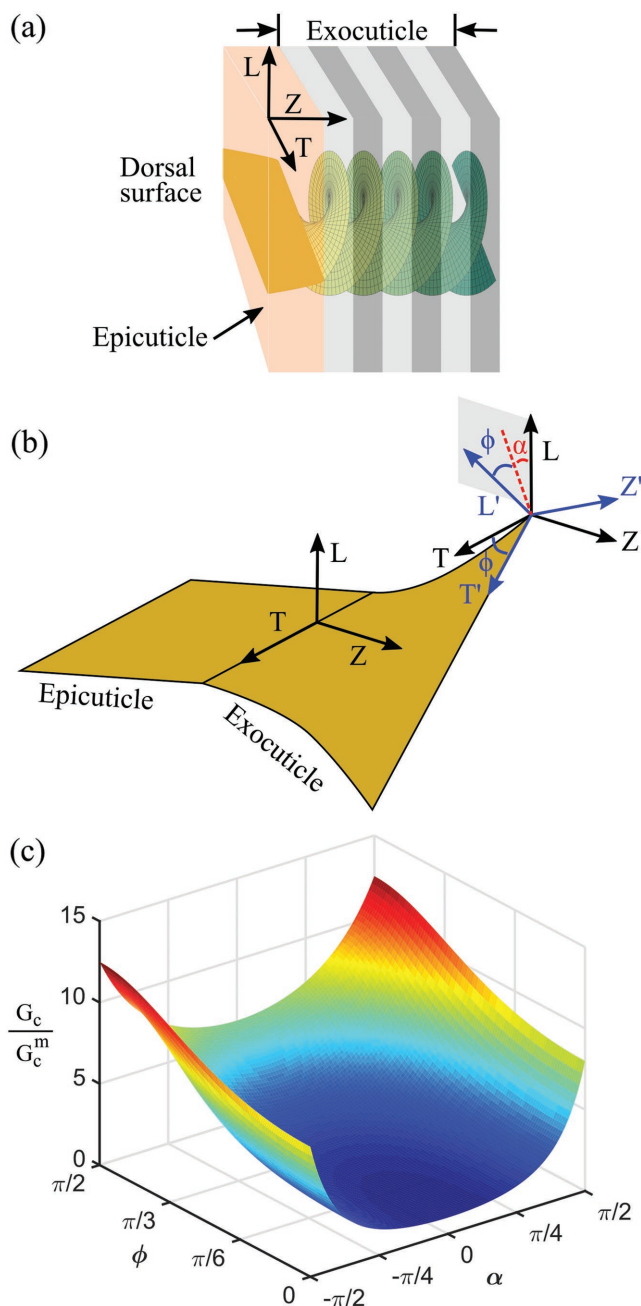


**Figure 3.** a) A Mode I crack in the epicuticle layer is shown. Upon further propagation into the procuticle, the crack follows a twisting path that is defined by the helicoidal structure of the exocuticle layer. b) A schematic of a crack transitioning from the epicuticle to exocuticle. Upon crossing into the exocuticle, the crack exhibits a twisting profile that matches the underlying helicoidal structure. The local material axes ( $L'$ - $T'$ - $Z'$ ) are defined as illustrated, and vary along the twisting crack profile. The kink ( $\alpha$ ) and twist ( $\varphi$ ) angles define the geometric relationship between the  $L$ - $T$ - $Z$  and  $L'$ - $T'$ - $Z'$  axes (see main text). c) The ratio of local ( $G_c$ ) to global ( $G_c^m$ ) fracture resistance in terms of the twist and kink angles of a twisting crack. This ratio is greater than 1 for all crack orientations, reflecting the potential improvements in Mode I fracture toughness due to mode mixity. At  $\alpha = 0$  and  $\varphi = 0$ , the twisting crack is locally under a pure Mode I loading condition.

and the related geometric parameters and axes. Noting that  $\alpha$  and  $\phi$  vary continuously along a twisting crack front, their local values can be described using the geometric relations for a helicoid, in the local material axes ( $L'$ – $T'$ – $Z'$ ). These axes are fixed using the following geometric constraints:  $T'$  is defined parallel to the local crack front,  $L'$  is defined as a unit normal to the local front, and  $Z'$  is the cross product of  $L'$  and  $T'$ . Under this definition of coordinate axes, the coefficients  $C_1$ ,  $C_2$ , and  $C_3$  can be calculated using the following relations<sup>[14]</sup>

$$C_1 = \cos(\alpha/2) \cdot [\cos^2(\alpha/2)\cos^2(\phi) + 2\nu\sin^2(\phi)] \quad (4a)$$

$$C_2 = \sin(\alpha/2) \cdot \cos^2(\alpha/2)\cos(\phi) \quad (4b)$$

$$C_3 = \cos(\alpha/2)\cos(\phi)\sin(\phi) \cdot [\cos^2(\alpha/2) - 2\nu] \quad (4c)$$

where  $\nu$  is determined from laminate homogenization to be 0.2. Based on this framework, Figure 3c depicts the relative enhancements in critical energy release rates for a twisting crack in the exocuticle of a figeater beetle. In this context,  $G_c^m$  refers to the intrinsic material resistance to the propagation of a straight crack under Mode I loading and  $G_c$  captures the apparent increase due to mode mixity effects. It can be observed that for all nonzero kink and twist angles,  $G_c/G_c^m$  is greater than one. This implies that higher applied forces are required for the crack to propagate, which results in higher resistance to predation. It should be noted that these improvements in the fracture resistance change at different positions along the crack front, as defined by the kink and twist angles. While this analysis highlights the potential improvements in fracture toughness that are achieved by imposing a helicoidal fracture path on a crack, we do not attempt an explicit determination of crack propagation in the beetle exoskeleton. Such fracture analysis would require full knowledge of the variations in the applied loadings along the crack front (i.e., local applied stress intensities). Currently, closed-form analytical solutions to these mechanics problems are absent in the literature. Finite element-based methods are emerging that can predict arbitrary crack deflection mechanisms

under multiaxial loadings. However, their applicability to anisotropic materials (such as helicoidal lamina) remains an open challenge to the community.<sup>[24]</sup>

It is pertinent to note that Nature uses a number of arrangements of mesoscale constituents to modulate fracture properties. For instance, recently Espinosa and co-workers<sup>[25]</sup> showed that pangolin scales possess a lamella organization, with a rotating morphology through the thickness. This organization strategy leads to modulation of the toughness through the thickness of the scale, with a higher toughness found in the ventral layers. By employing fracture and X-ray computerized tomography experiments, the work revealed that cracks follow a path outlined by the keratinous lamellae structure. In this respect, the origin and extent of toughening due to crack twisting in pangolin scales bears similarities to the beetle procuticle—highlighting the fact that Nature develops similar defense mechanisms from different building blocks in a diverse set of animals.

### 3. Biomimetic Helicoidal Composites—Effects of Pitch Angle on Stiffness and Toughness-

To further understand the effect of pitch angle on the mechanical behavior of helicoidal composites, we fabricated tensile test coupons (i.e., dog-bone shape) using 3D printing. We selected helicoidal structures with values of  $\gamma$  equal to 15°, 30°, 45°, 60°, 90°, and 180°, where the 45° sample corresponds to a [0/45/90/135] laminate, and the 180° corresponds to a unidirectional fiber composite, with the fibers aligned parallel to the loading direction. The selection of this set of pitch angles is intended to systematically probe the design space of the helicoidal motif—spanning from low-angle helicoids (i.e., as in the exocuticle of the figeater beetle,  $\gamma = 10.2^\circ$ – $16.4^\circ$ ) to traditional crossply laminates. Each sample possessed 12 layers through the gauge thickness, which provided an integral number of helicoidal pitches for each pitch angle. For example, 12 layers is equivalent to one helicoidal pitch in samples with  $\gamma = 15^\circ$ . Moreover, the helicoidal composites were deliberately designed with discontinuous fibers arranged with a 50% offset overlap (see Figure 4a). The purpose of this design is to avoid a

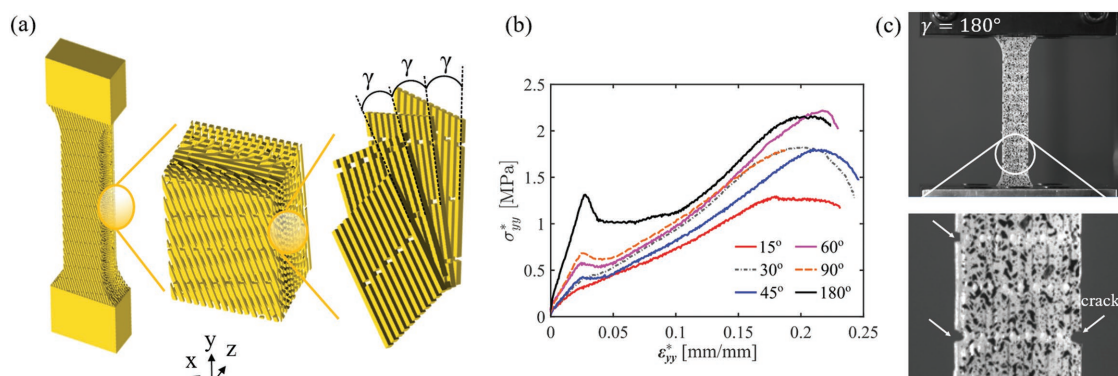


**Figure 4.** Effect of pitch angle  $\gamma$  on the mechanical performance of helicoidal composites with discontinuous fibers. a) Schematic representation of tensile test coupons for  $\gamma = 15^\circ$ . The insets highlight the short fibers and the pitch angle between reinforced layers. b) Stress–strain response of tested composites with  $\gamma$  equal to 15°, 30°, 45°, 60°, 90° and 180°.  $\sigma_{yy}^*$  and  $\epsilon_{yy}^*$  correspond to the far-field stresses and strains, respectively. c) Initial cracks between fibers for  $\gamma = 180^\circ$ . The formation of initial cracks between fibers causes the drop after the first stress peak.

distribution of fiber lengths through the thickness of the dog-bone, which arises from the intersection of rotated long-fiber laminae with the free surface. The discontinuous design implemented here avoids this undesirable complication and permits measurement of a representative volume element. This motif selection also fortuitously resulted in the combination of helicoidal and nacre-like structures. Nacre correspond to a brick and mortar-like architecture known for its high toughness and high stiffness, achieved through a cooperative sliding of mineral tablets, which spread inelastic deformation and suppress damage localization during loading.<sup>[2c,26]</sup> Therefore, we anticipate the combination of these two architectures will result in a richer failure mechanism arising from the combination of fiber pull-out and helicoidal cracking. Details of the fabrication and mechanical testing of these samples are provided in the Experimental Section and in the Supporting Information.

Representative stress–strain curves obtained from uniaxial tensile tests are shown in Figure 4b. The behaviors were found to be repeatable across several samples and at least three samples were tested for each helicoidal condition. The stress–strain curves for all samples tested in this study are provided in the Supporting Information. According to the results, the general behavior of all the samples is described by a linear stress–strain response up to a tensile strain between 2% and 3%. At this strain, the mechanical response reaches an inflection, where the subsequent hardening rates are observed to be inversely correlated to the helicoidal pitch angle. For example, the 45°, 60°, 90°, and 180° samples exhibit post-peak softening, followed by a plateau in the hardening behavior. This response is most evident in the 180° sample and is due to the formation of small notches between the fibers ends as shown in Figure 4c. Upon continued loading, the composites progressively harden up to ≈20% strain, after which the ultimate strength of the material is reached, followed by the complete failure of the samples. By comparison, the 15° and 30° samples exhibit continued strain hardening behavior post-inflection up to the ultimate tensile strength, albeit at a reduced hardening rate compared to the initial linear regime.

A close examination of the initial linear region observed in the stress–strain curves reveals that the initial elastic modulus increases proportionally with changes in the pitch angle as shown in Figure 5a. This behavior correlates with predictions from different analytical models used for composites. For instance, the most common model for the characterization of the tensile elastic modulus of composites with short discontinuous reinforcement is the Krenchel-shear lag model. In this model, the tensile elastic modulus can be computed by the following rule of mixtures

$$E_1 = K_0 K_1 E_f V_f + E_m V_m \quad (5)$$

with  $V_f$  and  $V_m$  corresponding to the volume fractions of the fibers and matrix respectively, and

$$K_0 = \sum_1^N \alpha_i \cos^4(\theta_i), \quad K_1 = 1 - \frac{\tanh(\beta l/2)}{\beta l/2}, \quad (6)$$

$$\beta = \frac{1}{r_f} \sqrt{\frac{G_m}{E_f} \left( \frac{2}{\ln(r_f/R)} \right)}$$

where  $l$  is the fiber length,  $r_f$  is the fiber radius, and  $R$  is the representative volume element radius. In this formulation,  $K_0$  is known as Krenchel's coefficient<sup>[27]</sup> or fiber orientation efficiency factor, which accounts for the proportion of fibers  $\alpha_i$  that have orientation  $\theta_i$  with respect to the loading direction.  $K_1$  is the shear lag or Cox's factor,<sup>[28]</sup> which is used for fiber length correction. Another model typically used for reinforced materials is laminate theory, where the reinforced material is considered as a stacking of fiber-reinforced laminae. In this model, the linear elastic modulus of the material is obtained by considering the local longitudinal ( $E_1$ ) and transverse ( $E_2$ ) elastic moduli of each individual lamina and the stacking orientation sequence.<sup>[29]</sup>

In Figure 5a the comparison between the elastic modulus measured experimentally and the predictions obtained using the Krenchel-shear lag model as well as laminate theory are presented. To calculate the elastic modulus using classical laminate theory, the homogenized elastic moduli of the lamina,  $E_1$  and  $E_2$ , were obtained from experimental measurements. These

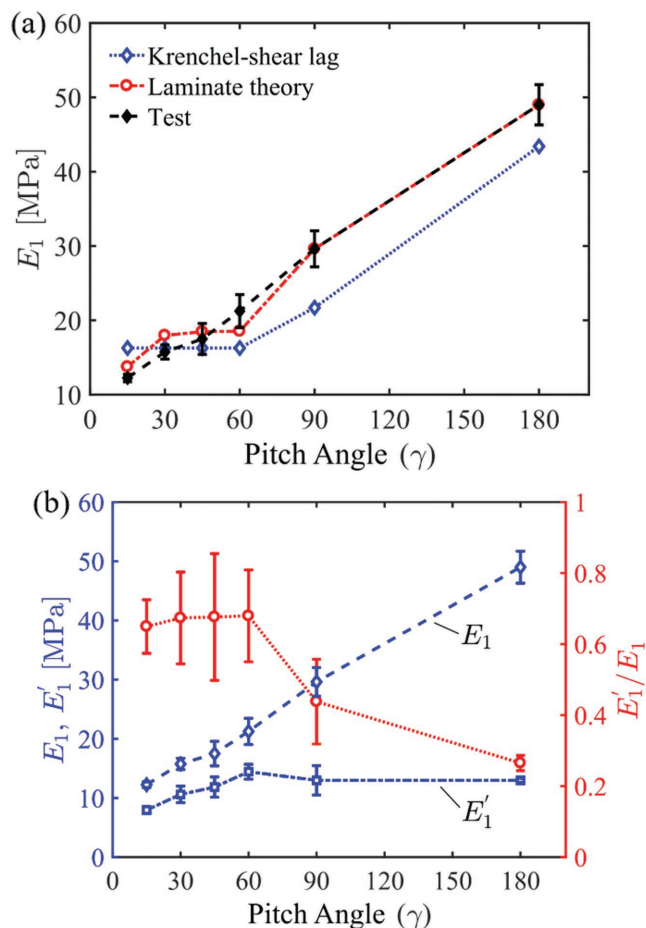


**Figure 5.** Effect of pitch angle ( $\gamma$ ) on the initial linear and post-peak behavior of helicoidal composites. a) Comparison between the initial elastic modulus ( $E_1$ ) characterized from experimental results and analytical models. b) Characterization of stiffness degradation  $E'_1/E_1$  in tested helicoidal composites. The values of  $E_1$  and the reduced modulus  $E'_1$  are also plotted for reference. Error bars in (a) and (b) represent one standard deviation measured over at least 3 samples.

values were taken from the 180° and 90° samples, and were measured to be 45 and 8 MPa, respectively. The lamina shear modulus  $G_{12}$  was calculated as 0.3 MPa using a Reuss model (i.e., series model) by taking the fiber Poisson's ratio as 0.4 and  $G_f$  as 369 MPa (calculated assuming an isotropic fiber material). From the figure, it is observed that the laminate theory model is able to accurately predict the decreasing trend of elastic modulus with reduction of helicoidal angle over the entire range of investigated pitch angles. In contrast, the Krenchel shear lag model saturates when the ply orientations become more evenly distributed within the laminate (e.g., in the case of helicoidal structures with  $\gamma$  to 15°, 30°, 45°, and 60°). This highlights the importance of considering both the effects of laminate asymmetry, included intrinsically in tailoring the laminate stiffness, and the effects of transverse and shear lamina elastic properties, which are absent in the Krenchel-shear lag model.

An interesting effect observed in the stress-strain curves corresponds to the stiffening occurring after the first peak stress. In order to characterize this effect, the reduced moduli  $E'_1$  was calculated by fitting a linear model within the interval  $\varepsilon_{yy}^* = (0.6-0.75) \varepsilon_{yy}^{\max}$  for all the stress-strain curves, where  $\varepsilon_{yy}^*$  represents the global far-field strain, and  $\varepsilon_{yy}^{\max}$  represents the strain at maximum global tensile stress. This range was found to adequately sample the secondary hardening range for all samples tested in this study. As observed in Figure 5b,  $E'_1$  remains approximately constant for all the values of  $\gamma$  ( $E'_1 = 10.29 \pm 1.62$  MPa). An approximately constant  $E'_1$  can be rationalized by the fact that in discontinuous fiber composites, equilibrium and compatibility invoke fiber-matrix shear load transfer after decohesion of the fiber ends. Interestingly, the ratio  $E'_1/E_1$ , which characterizes the stiffness degradation due to damage accumulation in composite materials,<sup>[21]</sup> exhibits an inverse relation with  $\gamma$  at higher pitch angles. Such relationship arises from the strong dependency of  $E_1$  on fiber orientation and the constancy of the reduced modulus  $E'_1$ . This implies that helicoidal composites with smaller pitch angles exhibit more moderate stiffness degradation. This behavior could be attributed to a redistribution of strain as a function of the helicoidal pitch angle. Another feature revealed by the present work is the strain heterogeneity, on the sample surface, as a function of pitch angle. To illustrate this, we plot the digital image correlation (DIC) strain maps along the loading direction ( $\varepsilon_{yy}$ ) in Figure 6a for all of the tested configurations of  $\gamma$  at a far-field applied strain of  $\varepsilon_{yy}^* = 0.13$ . It should be noted that the DIC maps show the surface strains in the terminal layers of the helicoid, whose fibers are oriented at an angle of  $\gamma$  to the loading axis. As observed in the strain fields, there is banding due to the orientation of discontinuous reinforcement, similar to the response reported in nacre.<sup>[26]</sup>

Furthermore,  $\gamma$  causes the orientation of the bands to change from oblique to horizontal for  $\gamma > 45^\circ$ . Movies showing the evolution of strain from DIC analysis are provided as the Supporting Information. Interestingly, examination of the statistical distribution of  $\varepsilon_{yy}$  over the sample surface (see Figure 6b) reveals that the local strain becomes more homogeneous as the helicoidal pitch angle approaches 60°. To interpret these measurements, we note that the 45° and 60° samples possess the largest proportions of unfavorably oriented fibers with respect to the loading direction. Moreover, the 45° and 60° samples are more symmetric in the sense that laminate symmetry is established within 2–3 layers, in contrast to the small pitch angle samples. The combined effect, under consideration of deformation compatibility and equilibrium, results in the observed narrow and broad  $\varepsilon_{yy}$  distributions. It is also worth noting that some authors have hypothesized that the post-peak stiffening observed during in the tests is related to a combined effect between matrix shearing and fiber reorientation.<sup>[30]</sup> However, a complete mechanistic understanding of this phenomenon has not been reported in the literature.

The DIC analysis can be complemented by examination of the fracture patterns in the samples after failure (Figure 7). Fractography analysis reveals that the dominant failure mechanism in all systems is matrix cracking. The

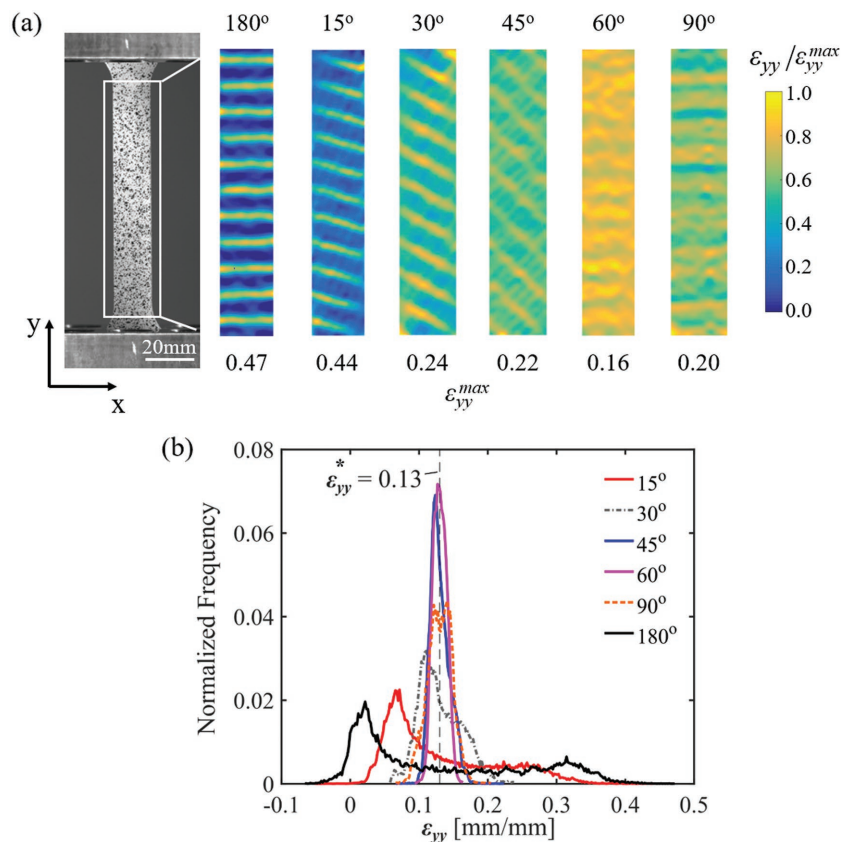


**Figure 6.** Strain heterogeneities in helicoidal composites during damage evolution. a) DIC images showing the local strain maps  $\varepsilon_{yy}$  at a global applied strain  $\varepsilon_{yy}^* = 0.13$  for all the tested helicoidal composites. The local strains have been normalized by their respective maximum values,  $\varepsilon_{yy}^{\max}$ , which are specified in the below each DIC map. b) Statistical distribution of  $\varepsilon_{yy}$  obtained from the strain field images.



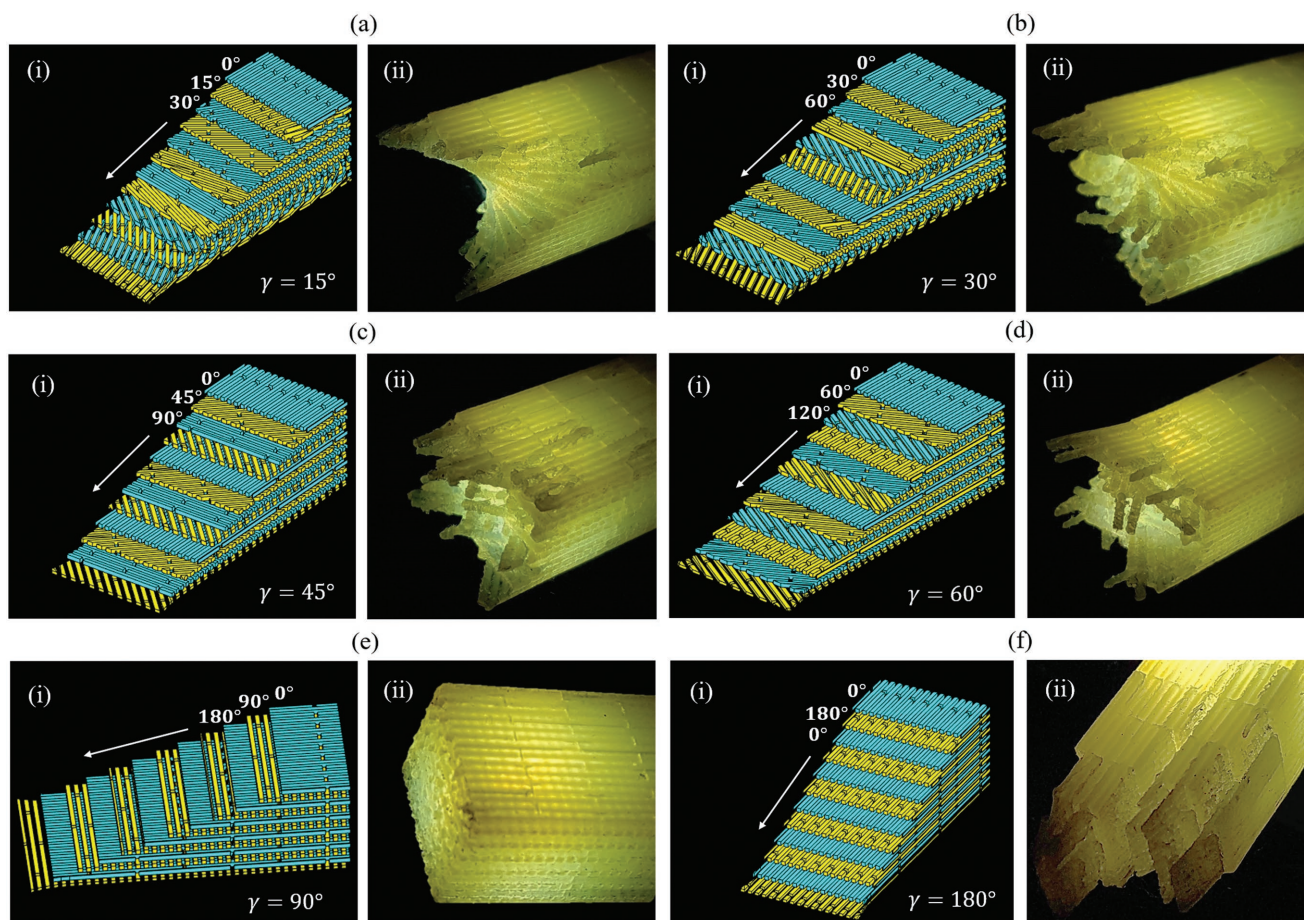


**Figure 7.** Overview of fractured surfaces in the tested helicoidal composites. a)  $\gamma = 15^\circ$ , b)  $\gamma = 30^\circ$ , c)  $\gamma = 45^\circ$ , d)  $\gamma = 60^\circ$ , e)  $\gamma = 90^\circ$ , f), and  $\gamma = 180^\circ$ . (i) and (ii) represent a schematic of the fiber layup and the fractogram, respectively.

fracture surfaces for both  $15^\circ$  and  $30^\circ$  systems clearly demonstrate twisting fracture paths that follow the spinning of fibers in the progressive layers of the helicoid (Figure 7a,b). This is more obvious for the former system in which the twisting angle is the lowest. In addition, the  $15^\circ$  sample has the least number of dangling fibers compared to other systems. The fibers of the  $45^\circ$  helicoidal angle sample are clearly noticeable from the fracture surface with the  $0^\circ$ ,  $45^\circ$ ,  $90^\circ$ , and  $135^\circ$  laminae being evident in Figure 7c. For the  $60^\circ$  helicoidal angle system, fiber pullout along different orientations is observed, with breakage and distortion occurring along with reorientation (Figure 7d). The lack of confinement near the sample surface is also apparent from the fiber orientation in these regions. The orthogonal laminate shows a brittle failure morphology with matrix cracking and failure of fibers oriented along the loading axis (Figure 7e). In the unidirectional case, Figure 7f, the failure occurs by separation of columnar stacks of fibers (nacre-like). This is because adjacent fibers in each lamina are stacked in a discontinuous pattern (fiber staggering) in contrast to a continuous stacking of layers, which mitigates the formation of through-thickness matrix cracks.

Although helicoidal structures do not exhibit the same mechanical performance as unidirectional composites, helicoids present a good compromise for design cases where

the loading conditions are unknown a priori due to their higher degree of isotropy. Also, the combination of helicoidal and nacre-like motifs allows for a better redistribution of the deformation, which permits the material to better prevent localized damage accumulation and provide more effective mechanisms for load transfer. These mechanisms are noted in more traditional composites with  $\gamma = 45^\circ$  and  $\gamma = 60^\circ$ . Therefore, more comprehensive analyses considering the geometry of the fibers, the thickness of the plies and different combinations of materials are required in order to understand the trends observed in nature where helicoidal composites with lower  $\gamma$  are preferred.

#### 4. Conclusions

The ubiquity of helicoidal structures in the animal and the plant kingdoms underscores their importance as an adaptable motif that enable a multitude of functionalities. To uncover how nature uses the helicoidal structure as a template for adaptable mechanical niches, the figeater beetle exoskeleton is examined at two different developmental stages—namely the larva and adult stages. In the larval stage, the double helicoid structure of the beetle cuticle serves a primarily protective role. During

development, the beetle exoskeleton undergoes structural changes to form an adult elytron comprised of helicoidal and pseudo-helicoidal features. Our results suggest that the adult elytron provides higher stiffness while maintaining protective features to defend the soft inner wings and body from predation. More specifically, the exocuticle (outer layer) of the elytron appears optimized for damage tolerance, and the endocuticle (inner layer) for structural stiffness.

To complement our understanding of the helicoidal architecture as an adaptable material system, 3D printing was utilized to fabricate synthetic helicoids for a systematic mechanics study of deformation and fracture. The manufactured helicoidal fibrous systems, in which only the pitch angle between layers was changed, were tested under uniaxial tensile loading. The mechanical response of these synthetic composites exhibited elasticity, inelasticity, and failure with a strong dependence on pitch angle. Comparison between predictions from theoretical models and test data revealed the ranges of validity for popular models and their utility in helicoidal composite material design. Furthermore, analysis of the stress–strain data showed an overall pronounced stiffness reduction during inelastic deformation when the pitch angle is increased. DIC analysis was used to examine strain heterogeneities during tensile loading. Off-axis fiber orientation distribution and number of layers require to achieve lamina symmetry are found as key factors in achieving homogeneous deformations. Moreover, post-mortem analysis reveals a fracture pathway delineated by the twisting features of the underlying helicoid structure. Smaller pitch angles resulted in fracture morphologies with more clearly defined helicoidal patterns.

We close by noting that Nature can achieve high performance mechanical architectures through efficient phase organization and constituent selection. While progress in biomimicry of natural materials has been significant, architecture control with the desired spatial distribution of constituents remains a major challenge. In this work, we show that additive manufacturing offers promising capabilities to control constituent chemistries, dimensions, as well as structural motifs to achieve tailored mechanical properties. In this regard, we envision that the outcome of this research will pave the way for bioinspired design adaptable fibrous composite systems that can subsequently shed light on how Nature has evolved materials to optimize mechanical properties.

## 5. Experimental Section

The composites were fabricated in a Stratasys Connex350 3D printer using a rigid polymer (VeroWhite,  $E_f = 1032.25 \pm 184.45$  MPa) for the fibers, and a soft rubber-like polymer (TangoPlus,  $E_m = 0.3 \pm 0.05$  MPa,  $G_m = 0.2 \pm 0.05$  MPa) for the matrix, which correlates with the trends observed in nature for this type of structures.  $E$  and  $G$  refer to the elastic and shear moduli, and the subscript indicates the fiber (f) or matrix (m) constituents, respectively. The details regarding the characterization of the base materials are presented in the Supporting Information. The grip sections of the samples were printed of pure VeroWhite to prevent stress concentrations and damage during clamping of the samples to the testing machine. The composite tensile test coupons have a gauge section measuring 56.4 mm in length, 14.1 mm in width, 10.8 mm in thickness, and a fillet radius between the tab and gauge of 15 mm. The discontinuous fibers in the composite are printed with a length of

10 mm and a square cross-section of 0.5 mm  $\times$  0.5 mm. In addition, the interspacing distance between fibers in all directions was set to 0.4 mm. Under these dimensions, each layer is nominally 0.9 mm thick and each helicoidal composite possesses 12 layers through the coupon thickness. While the theoretical volume fraction of the fibers with these parameters corresponds to 30%, further measurements on the printed samples revealed a real volume fraction of 35.5%. The difference between nominal and measured volume fractions is attributable to fiber-matrix material diffusion during the printing process due to the printer resolution limitations. Finally, the printed composites were tested under quasi-static tensile loading (strain rate of  $8 \times 10^{-4}$  s $^{-1}$ ) in a universal testing machine (MTS Dual Column Testing Systems, USA). For all tests, the loading direction was parallel to fibers of the first layer printed in the helicoid. Fiber orientation in subsequent layers is defined by the pitch angle of each specimen. Due to the selected pitch angles and pitch thickness, the terminal pitch layers are oriented at an angle of  $\gamma$  to the loading axis. Strain mapping during testing was determined using DIC. All strains in DIC analysis correspond to the Green formulation.

## Supporting Information

Supporting Information is available from the Wiley Online Library or from the author.

## Acknowledgements

The authors gratefully acknowledge financial support from a Multi-University Research Initiative through the Air Force Office of Scientific Research (AFOSR-FA9550-15-1-0009). The authors also thank the support provided by Dr. Hugh DeLong and Dr. Sofi Bin-Salamon. B.R. was supported by a Ministry of Defense/Royal Academy of Engineering Research Fellowship. This work made use of the Central Laboratory for Materials Mechanical Properties supported by the MRSEC program of the National Science Foundation (DMR-1121262) at the Northwestern University Materials Research Science and Engineering Center. M.D. would like to acknowledge financial support under the Postdoctoral Fellowships Program (Application No.: PDF-502224-2017) from the Natural Sciences and Engineering Research Council (NSERC) of Canada.

## Conflict of Interest

The authors declare no conflict of interest.

## Keywords

3D printing, beetle exoskeletons, fracture mechanics, helicoidal composites, laminate theory

Received: May 3, 2018

Revised: May 23, 2018

Published online: June 25, 2018

- [1] a) H. D. Espinosa, J. E. Rim, F. Barthelat, M. J. Buehler, *Prog. Mater. Sci.* **2009**, *54*, 1059; b) X. Wei, M. Naraghi, H. D. Espinosa, *ACS Nano* **2012**, *6*, 2333; c) X. Wei, T. Filleter, H. D. Espinosa, *Acta Biomater.* **2015**, *18*, 206; d) J. W. Dunlop, Y. J. Brechet, *MRS Online Proc. Libr.* **2009**, 1188; e) M. Ashby, *Scr. Mater.* **2013**, *68*, 4; f) Y. Brechet, J. D. Embury, *Scr. Mater.* **2013**, *68*, 1.
- [2] a) M. A. Meyers, P. Y. Chen, A. Y. M. Lin, Y. Seki, *Prog. Mater. Sci.* **2008**, *53*, 1; b) U. G. K. Wegst, H. Bai, E. Saiz, A. P. Tomsia,

- R. O. Ritchie, *Nat. Mater.* **2015**, *14*, 23; c) F. Barthelat, H. Espinosa, *Exp. Mech.* **2007**, *47*, 311.
- [3] S. E. Naleway, M. M. Porter, J. McKittrick, M. A. Meyers, *Adv. Mater.* **2015**, *27*, 5455.
- [4] P. Y. Chen, J. McKittrick, M. A. Meyers, *Prog. Mater. Sci.* **2012**, *57*, 1492.
- [5] N. Du, Z. Yang, X. Y. Liu, Y. Li, H. Y. Xu, *Adv. Funct. Mater.* **2011**, *21*, 772.
- [6] T. Ikoma, H. Kobayashi, J. Tanaka, D. Walsh, S. Mann, *J. Struct. Biol.* **2003**, *142*, 327.
- [7] B. D. Wilts, H. M. Whitney, B. J. Glover, U. Steiner, S. Vignolini, *Mater. Today: Proc.* **2014**, *1*, 177.
- [8] M. Mitov, *Soft Matter* **2017**, *13*, 4176.
- [9] Y. Bouligand, *C. R. Acad. Sci.* **1965**, *261*, 3665.
- [10] a) A. C. Neville, B. M. Luke, *J. Insect Physiol.* **1971**, *17*, 519; b) S. A. Jewell, P. Vukusic, N. W. Roberts, *New J. Phys.* **2007**, *9*, 99.
- [11] A. Bigi, M. Burghammer, R. Falconi, M. H. Koch, S. Panzavolta, C. Riek, *J. Struct. Biol.* **2001**, *136*, 137.
- [12] R. G. Yang, A. Zaheri, W. Gao, C. Hayashi, H. D. Espinosa, *Adv. Funct. Mater.* **2017**, *27*, 1603993.
- [13] R. A. Muzzarelli, *Chitin*, Pergamon Press, New York, USA **1977**.
- [14] N. Suksangpanya, N. A. Yaraghi, D. Kisailus, P. Zavattieri, *J. Mech. Behav. Biomed. Mater.* **2017**, *76*, 38.
- [15] S. Nikolov, M. Petrov, L. Lymperakis, M. Friak, C. Sachs, H. O. Fabritius, D. Raabe, J. Neugebauer, *Adv. Mater.* **2010**, *22*, 519.
- [16] M. C. Verkerk, J. Tramper, J. C. M. van Trijp, D. E. Martens, *Biotechnol. Adv.* **2007**, *25*, 198.
- [17] a) S. Caveney, *J. Insect Physiol.* **1970**, *16*, 1087; b) A. C. Neville, *Biology of Fibrous Composites: Development beyond the Cell Membrane*, Cambridge University Press, New York, USA **1993**.
- [18] B. Zelazny, A. C. Neville, *J. Insect Physiol.* **1972**, *18*, 2095.
- [19] L. Cheng, L. Y. Wang, A. M. Karlsson, *J. Mater. Res.* **2009**, *24*, 3253.
- [20] L. Frantsevich, Z. D. Dai, W. Y. Wang, Y. F. Zhang, *J. Exp. Biol.* **2005**, *208*, 3145.
- [21] I. M. Daniel, *Engineering Mechanics of Composite Materials*, Oxford University Press, New York **2005**.
- [22] S. I. Ranganathan, M. Ostoja-Starzewski, *Phys. Rev. Lett.* **2008**, *101*, 055504.
- [23] J. F. Vincent, *Structural Biomaterials*, Princeton University Press, New Jersey, USA **2012**.
- [24] a) P. Gupta, C. Duarte, *Int. J. Numer. Anal. Methods Geomech.* **2014**, *38*, 1397; b) P. Gupta, C. Duarte, A. Dhankhar, *Eng. Fract. Mech.* **2017**, *179*, 120.
- [25] M. J. Chon, M. Daly, B. Wang, X. H. Xiao, A. Zaheri, M. A. Meyers, H. D. Espinosa, *J. Mech. Behav. Biomed. Mater.* **2017**, *76*, 30.
- [26] a) H. D. Espinosa, A. L. Juster, F. J. Latourte, O. Y. Loh, D. Gregoire, P. D. Zavattieri, *Nat. Commun.* **2011**, *2*, 173; b) J. E. Rim, P. Zavattieri, A. Juster, H. D. Espinosa, *J. Mech. Behav. Biomed. Mater.* **2011**, *4*, 190.
- [27] H. Krenchel, *Fibre Reinforcement*, Alademisk forlag, Copenhagen, Denmark **1964**.
- [28] H. L. Cox, *Br. J. Appl. Phys.* **1952**, *3*, 72.
- [29] J. N. Reddy, *Mechanics of Laminated Composite Plates and Shells: Theory and Analysis*, CRC Press, New York, USA **2004**.
- [30] E. A. Zimmermann, B. Gludovatz, E. Schaible, N. K. N. Dave, W. Yang, M. A. Meyers, R. O. Ritchie, *Nat. Commun.* **2013**, *4*, 2634.